Journal of Power Sources 231 (2013) 246–255

Contents lists available at SciVerse ScienceDirect

Journal of Power Sources

journal homepage: www.elsevier.com/locate/jpowsour

Operating conditions affecting the contact resistance of bi-polar plates in proton exchange membrane fuel cells

Alejandro Oyarce [a,*], Nicklas Holmström [a], Andreas Bodén [b], Carina Lagergren [a], Göran Lindbergh [a]

[a] Department of Chemical Engineering and Technology, Applied Electrochemistry, KTH Royal Institute of Technology, SE-10044 Stockholm, Sweden
[b] PowerCell Sweden AB, SE-418 34 Gothenburg, Sweden

HIGHLIGHTS

- The contact resistance of different BPP materials was measured ex-situ and in-situ.
- Contact resistance decreases with increasing temperature and humidity of gases.
- Contact resistance increases with increasing current density and time.
- Contact resistance increases due to the presence of liquid water.

ARTICLE INFO

Article history:
Received 24 September 2012
Received in revised form
17 December 2012
Accepted 27 December 2012
Available online 5 January 2013

Keywords:
PEM fuel cell
Contact resistance
In-situ
Bi-polar plate
Stainless steel
Durability

ABSTRACT

Both ex-situ and in-situ measurements of contact resistance between gas diffusion layer (GDL) and bi-polar plate (BPP) were carried out using the same fuel cell hardware. Each BPP sample was submitted to ex-situ testing at room temperature, ex-situ testing in simulated fuel cell environment and in-situ testing, isolating the effect of specific operating conditions on the contact resistance. Increasing cell temperatures and relative humidity (RH) of the gases lowered the contact resistance. However, the presence of liquid water, measured as an increase in pressure drop over the cathode, affected the contact resistance negatively. High current density operation raises the temperature of the cell, but simultaneously increases the water content at the cathode, causing an increase of the contact resistance. In the case of uncoated steel 316L and gold-coated steel 316L, high current density operation for an extended period of time also caused a progressive deterioration of the contact resistance, which without this in-situ measurement could have been mistaken for other ohmic losses, e.g. increased membrane resistance due to metal ion poisoning.

© 2013 Elsevier B.V. All rights reserved.

1. Introduction

The primary function of bi-polar plates (BPPs) in a fuel cell stack is to distribute and separate the fuel and the oxidant stream within the cell. BPPs also have to assist in the water management, the transport of heat, as well as function as current collectors and mechanical support. Graphite and graphite composite materials have traditionally been used as BPPs in proton exchange membrane fuel cells (PEMFCs) because these materials fulfill two of the most important requirements for BPPs, namely high corrosion resistance and low contact resistance [1]. However, due to these materials' high gas permeability and lack of mechanical strength, PEMFC stacks using graphite BPPs may become very bulky, creating the need for alternative materials [2–4]. Stainless steels have emerged as the most used material due to the possibility of mass producing extremely thin plates. On the other hand, concerns as to the chemical instability of stainless steels when exposed to fuel cell environment [5,6] and the formation of passive films on the surface of the steels that may increase the contact resistances in the fuel cell [7,8] have led to intense research in the field of stainless steel coatings [9–11] and stainless steel surface modifications [12,13]. The evaluation of new BPP materials is therefore usually carried out in terms of both corrosion resistance and contact resistance [7,14,15].

The focus of this study, however, is solely aimed at studying the contact resistance between GDL and BPP and specifically how different fuel cell conditions might affect this particular ohmic loss. The contact resistance is commonly measured using ex-situ methods, such as the one developed by Davies et al. [3] and later modified by Wang et al. [7]. By measuring the total voltage drop (E)

* Corresponding author. Tel.: +46 763414275; fax: +46 8249366.
E-mail address: alob@kth.se (A. Oyarce).

0378-7753/$ – see front matter © 2013 Elsevier B.V. All rights reserved.
http://dx.doi.org/10.1016/j.jpowsour.2012.12.100

through these setups and at the same time controlling the clamping pressure (P_c), it is possible to calculate the total resistance as a function of clamping pressure according to Ohm's law:

$$R_{tot}(P_c) = \frac{EA_s}{I} \quad (1)$$

where R_{tot} is the total area specific resistance through the setup, A_s is the area of the sample and I is the total applied current. These ex-situ measurements are expeditious, relatively inexpensive and constitute a practical way of performing fast screening among candidate BPP materials in terms of contact resistance. On the other hand, these experiments are most commonly carried out at room temperature and in air, failing to predict possible changes in contact resistance due to the fuel cell environment.

Several research groups have indeed tested alternative BPPs and coating materials inside PEMFCs [2–6,8,9,11,16]. These in-situ trials are of course essential for evaluating the overall performance, as well as the long-term stability of the fuel cell. However, it has been noticed that when different BPP materials are compared in-situ, the differences in fuel cell performance do not always correlate with the differences in ex-situ contact resistance [3,4,16–18]. Perhaps equally challenging is to determine the origin of losses generated during long periods of operation. Changes in contact resistances can be very difficult to identify and separate from other possible ohmic losses such as membrane resistance or electrode ionomer resistances, even when applying electrochemical impedance spectroscopy (EIS) as characterization method [19].

To the authors' knowledge, only a few groups have specifically evaluated the in-situ contact resistance between BPP and GDL [20–22]. Makkus et al. [20] showed that the anode-side stainless steel plates had lower contact resistances than the cathode-side plates. Additionally, the cathode-side contact resistance was shown to increase during operation. Due to the fuel cell design, the study was only able to control the total compaction pressure to seal the cell and because some of this pressure went to compress the sealing, it made it difficult to attain reliable values of contact resistances. Ihonen et al. [21] developed a fuel cell design that was able to separate clamping pressure from the sealing pressure and measured the contact resistance of platinum coated and uncoated SS136 stainless steel as function of clamping pressure, current density, gas pressure and operating time. The study concludes that the contact resistance of uncoated 316L is not stable, that it might alter to a new level after changes in operating conditions. In an earlier report Oyarce et al. [22] performed both the ex-situ and in-situ measurements with flat stainless steel samples and observed that the contact resistance increases during operation. Furthermore, the increase in contact resistance was larger for the uncoated 316L steel than for the uncoated 904L steel.

The aim of this study is to pinpoint more precisely which fuel cell operating conditions may cause changes in contact resistance. This is achieved by gradually changing the environment at which the measurements are carried out, using the same experimental set-up and the same BPP sample. Ex-situ measurements at room temperature are carried out for the initial evaluation of the contact resistance of different BPP materials and the effect of various types of GDLs. Ex-situ measurements in simulated fuel cell environment are used to isolate the effect of current density, temperature and water, without having the influence of the MEA. Finally, in-situ measurements provide the contact resistance of the materials under the same conditions as the previous experiments, however adding the dynamic changes provided by the fuel cell, e.g. combined water and heat production at the cathode and thickness variations of membrane.

2. Experimental

2.1. Fuel cell hardware

All measurements were performed in a modified version of Ihonen's et al. [21,22] fuel cell design. The two most important features of the in-house cell design are: *i*) the clamping pressure is separated from the sealing pressure, allowing the precise control of the compression between BPP and GDL and *ii*) the construction material of the cell body is polyether-ether ketone (PEEK), this electrically insulating material allows the installation of probes to measure the potential. This novel PEMFC is to the author's knowledge, the only fuel cell design that allows a straightforward assembly of the fuel cell, as well as reproducible and reliable measurements of the in-situ contact resistance between GDL and BPP. The cell has two movable cylindrical current collectors made of graphite KC-673 (Svenska Tanso AB) with an active area and flow field of 7 cm^2. The temperature was measured and controlled with a K-type thermocouple placed 1 mm away from the gas outlet of the current collectors and the heat was supplied by four heating elements inserted in the PEEK cell body. The gases were humidified with Milli-Q water by a fuel cell test station (Globe Tech Inc.) and the gas flow rates were controlled by mass flow controllers (Brooks Instruments B. V.). To avoid condensation between test station and fuel cell, the temperature of the connecting pipes was in all cases 5 °C higher than the dew point temperature. The clamping pressure was regulated by a pressure controller (Brooks 5866) connected to a pneumatic piston (Rexroth Mecman Pneumatic), where the maximum clamping pressure on the 7 cm^2 area was 14 bar (140 N cm^{-2}). The BPP samples had a spiral flow field where the total land area was 3.86 cm^2 for the graphite current collector and 3.82 cm^2 for the uncoated 316L and gold-coated 316L samples. The channel depth was 1 mm for graphite and 0.4 mm for the two stainless steel samples.

2.2. Ex-situ contact resistance

Fig. 1a illustrates how each BPP sample and a circular 10 cm^2 GDL were placed between the graphite current collectors. Two platinum probes (Probe I and Probe II) were used to contact the GDL and ensure that all changes in contact resistance were probe-independent. Furthermore, these potential probes were inserted through the cell body and were placed less than 1 mm away from the active area to minimize the measurement error [21]. The stainless steel samples were contacted through a hole in the graphite current collector using a platinum probe (Probe III) insulated with a thin alumina tube [23]. The voltage drop between GDL (Probe I and Probe II) and BPP (Probe III) was continuously measured by a data acquisition/switch unit (Agilent). Additionally, the voltage drop between the GDL and current collector A, GDL and current collector C, as well as the voltage drop between current collectors A and C were also measured and recorded continuously. A constant current density of 0.143 A cm^{-2} (1 A) was applied with a PGSTAT30 (Autolab) connected to a 10 A booster (BSTR10A) and the voltage drop was recorded at 2, 4, 6, 8, 10 and 12 bar clamping pressure for 5 min at each clamping pressure.

2.3. Ex-situ contact resistance in simulated environment

Fig. 1b shows a schematic picture of the modifications made to the experimental set-up to allow the study of the contact resistance dependence on current density, temperature and the presences of water. A piece of electronically conductive Papyex® Graphite Foil (Carbon Nordic AB) was used to separate the two compartments and measure the pressure drop though the flow field/GDL using

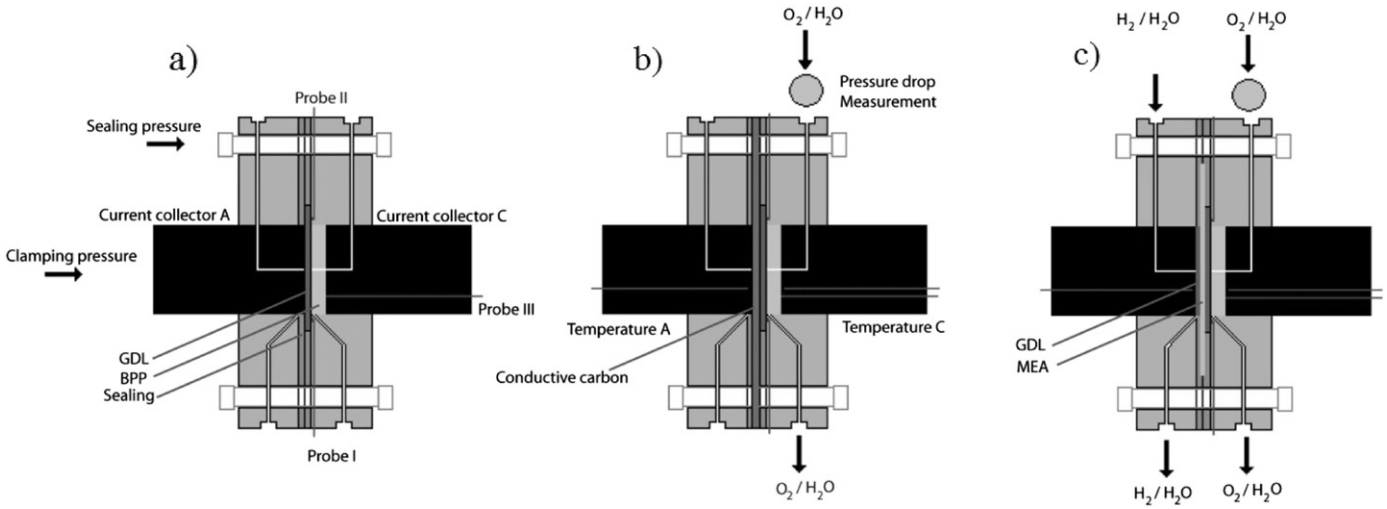

Fig. 1. Schematic drawing of the experimental set-up used for the: a) ex-situ contact resistance, b) ex-situ contact resistance in simulated environment and c) in-situ contact resistance.

a 400 mbar pressure meter/controller (Bronkhorst). A flow rate of 60 ml min^{-1} of O_2 (99.999% AGA AB) was used.

2.4. In-situ contact resistance

As pointed out earlier, the in-situ measurements were performed using the previously tested BPP samples and using the same fuel cell hardware, see Fig. 1c. The gas flow rates were also the same as for the previous experiments. MEAs 35 μm PRIMEA Series 5621 MESGA (W. L. GORE & Associated, Inc.) with platinum loadings of 0.45 mg cm^{-2} on the anode and 0.6 mg cm^{-2} on the cathode were used. For each BPP sample, a new MEA was sandwiched between two fresh pieces of GDL material (SIGRACET® 10 BC) and the contact resistance dependence on temperature, gas RH, current density and time was studied and compared to the ex-situ measurements in simulated environment. EIS measurements were performed using an IM6 unit together with an EL101 Booster (Zahner Elektrik). The frequency range was 10 kHz–100 mHz and the amplitude 50 mA. The total ohmic resistance of the cell, also denoted high frequency resistance (HFR), is taken from the real impedance at 1 kHz.

3. Results

3.1. Ex-situ contact resistance

Fig. 2 depicts both the contact resistance (resistance normalized to the total area of the BPP) and the area-specific contact resistance (resistance normalized to the land area of the BPP) of an uncoated 316L steel and a graphite sample using GDL SIGRACET® 10 BC. The measurements show the typical dependence of the contact resistance on the clamping pressure, where increasing clamping pressures result in the deformation of the GDL and the creation of more contact points at the BPP/GDL interface. The GDL deformation increases the effective contact area and results in the decrease of the contact resistance. The graphite sample not only shows one order of magnitude lower contact resistance than uncoated 316L, but has also a smaller percentage decrease of the contact resistance, meaning that each additional contact point between BPP and GDL is more significant for the uncoated 316L steel. Consequently, contact resistance measurements using poorly conducting BPP materials will not only be more sensitive to changes in the effective contact area, but will also decrease the reproducibility of the measurement.

From Fig. 2 it is possible to observe that while the contact resistance of graphite at 8 bar is 12 ± 1 mΩ cm^2, the contact resistance of uncoated 316L is 160 ± 20 mΩ cm^2.

It has previously been shown that the effective contact area between steel and GDL could significantly be increased by increasing the surface roughness of the steel [13]. Fig. 3 shows that the type of GDL can also be used as a strategy to maximize the effective contact area. At a clamping pressure of 8 bar, the contact resistance varies from 110 mΩ cm^2 using a GDL such as SIGRACET® 10 BA to approximately 290 mΩ cm^2 using a GDL such as SIGRACET® 20 BC.

Fig. 4 shows the structure and morphology of some of these GDLs and may serve as an illustrative indication of the large disparities in contact resistance when using different GDLs. It becomes apparent that a thin, low porous GDL such as SIGRACET® 20 BC that in addition includes a micro porous layer (MPL) in its structure

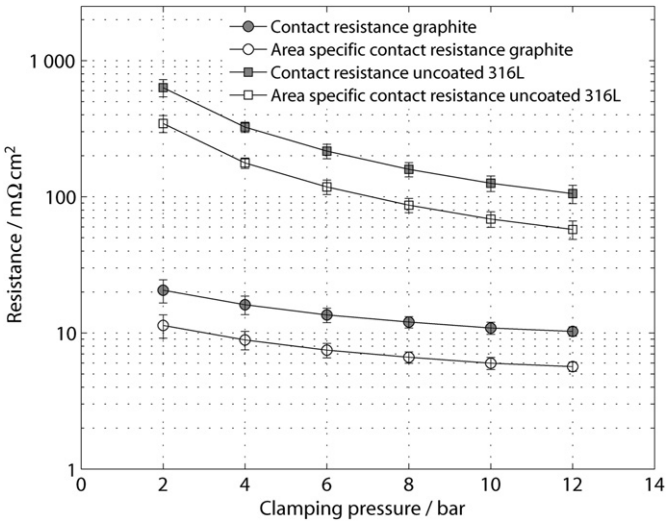

Fig. 2. Ex-situ contact resistance of uncoated 316L steel and graphite at room temperature (23 °C), using Sigracet 10 BC and applying a current density of 0.143 A cm^{-2}. The contact resistance is calculated with Eq. (1) where the total area of the BPPs is 7 cm^2, the land area of graphite BPP is 3.86 cm^2 and the land area of uncoated 316L is 3.82 cm^2. The error bars are obtained from five individual measurements using the same BPP sample and fresh GDLs.

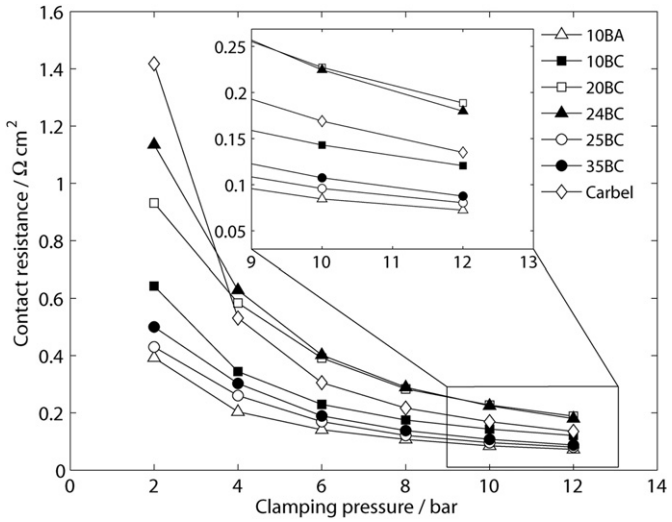

Fig. 3. Effect of GDL on the ex-situ contact resistance of uncoated 316L steel at room temperature (23 °C) and current density 0.143 A cm^{-2}. The contact resistance is calculated with Eq. (1) using the total area of the BPP (7 cm^2).

cannot be compressed to the same extent as a thicker, more porous GDL such as SIGRACET® 10 BA. It is however worth pointing out that the GDL plays a crucial role in the heat-and water-management of the fuel cell, as well as in the gas phase transport; thus it is important that the choice of GDL is instead carried out considering the optimization of the overall fuel cell performance at the particular conditions of operation and not only optimized as function of contact resistance [24].

Fig. 5a shows the great advantage of applying a good electronically conductive coating. The coating reduces the contact resistance of 316L to the same order of magnitude as the graphite current collector (35 mΩ cm^2 at 8 bar). In contrast to uncoated 316L, where large amounts of contact points are needed at the interface to have a relatively good conduction, gold-coated 316L conducts very well even when the contact points are few. This can clearly be observed in Fig. 5b where the contact resistance of gold-coated 316L is measured using different GDLs. As a result of the high conductivity of gold, together with the plane contact between the gold coating and the steel substrate, the type of GDL has only a minor effect on the contact resistance.

3.2. Ex-situ contact resistance in simulated environment

Current density is an operating parameter that unavoidably will be varied in a fuel cell. Fig. 6 shows that the contact resistance between uncoated 316L and SIGRACET® 10 BC decreases with both

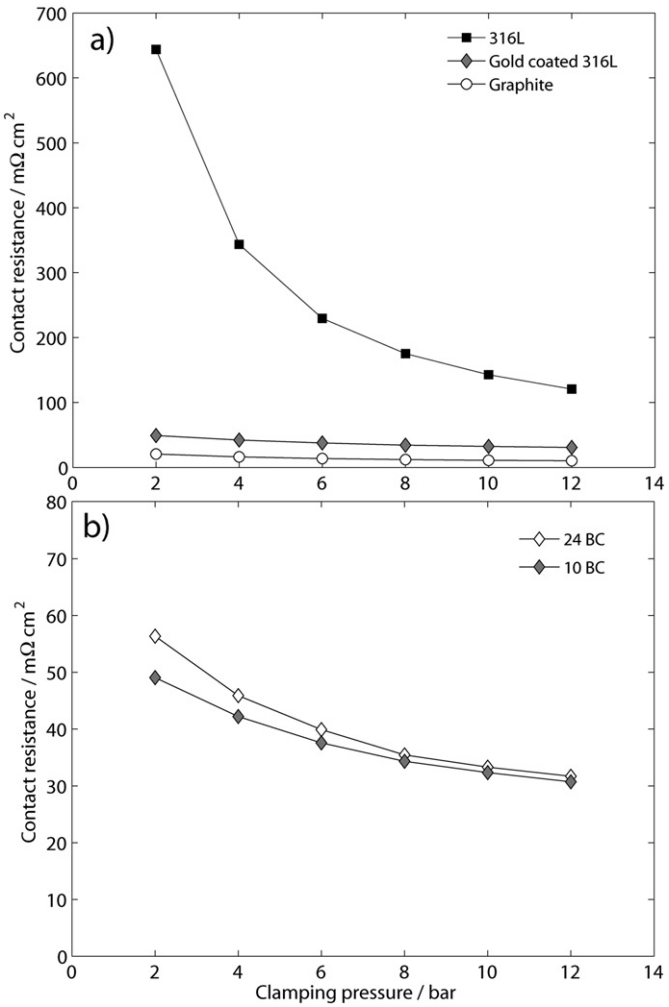

Fig. 5. Ex-situ contact resistance at room temperature (23 °C) applying a current density of 0.143 A cm^{-2}. The contact resistance is calculated with Eq. (1) using the total area of the BPP (7 cm^2). a) Effect of coating on steel 316L using Sigracet 10 BC and b) effect of GDL on the ex-situ contact resistance of gold-coated 316L.

clamping pressure and current density. At a clamping pressure of 2 bar the percentage decrease of the contact resistance is as large as 45% when the current density is stepped up from 0.07 A cm^{-2} to 1 A cm^{-2}. At a clamping pressure of 12 bar, on the other hand, the decrease is only about 10%. This result indicates that the current density has only a small impact on the contact resistance when the effective contact area is maximized during assembly.

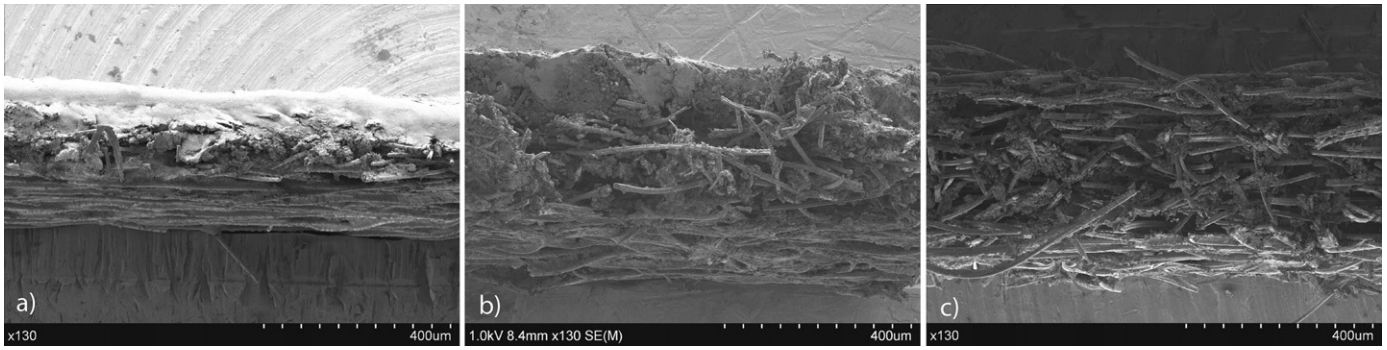

Fig. 4. SEM images of: a) 20 BC, b) 10 BC and c) 10 BA.

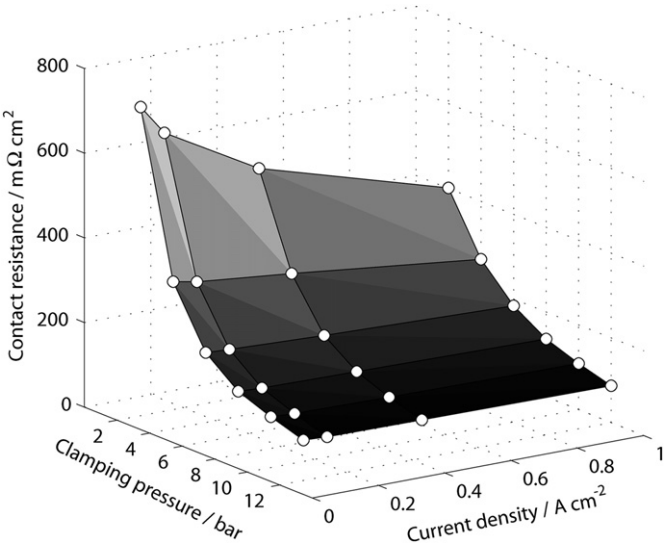

Fig. 6. The effect of current density on the ex-situ contact resistance of uncoated 316L using GDL Sigracet 10 BC. The measurement is performed at room temperature (23 °C) and each point is the mean value of a 5 min measurement.

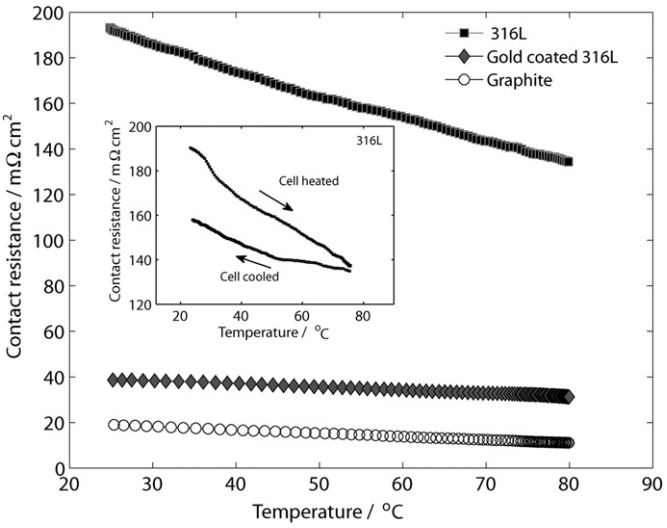

Fig. 8. Effect of temperature on the ex-situ contact resistance of uncoated 316L, clamping pressure 8 bar, GDL Sigracet 10 BC and constant current density 0.143 A cm^{-2}. The inset shows a separate measurement of the contact resistance of uncoated 316L during the forward and backward temperature sweep.

It is well established that the interfacial thermal resistance between BPP and GDL follows a similar dependence on clamping pressure as the contact resistance. A small effective contact area between these two components will results in larger thermal resistances and will therefore generate more ohmic heat for any given current density. Fig. 7 shows the transient of the measurements carried out at 2 bar and 12 bar from Fig. 6. The measurements start at room temperature, however as the current density is increased; the generated ohmic heat increases the temperature of the cell. Even more interesting however, is that every transient increase in temperature seems to be accompanied by a transient decrease of the voltage drop between BPP and GDL. It is therefore suggested that the contact resistance may be dependent on current density through its dependence on temperature.

Fig. 8 shows the contact resistance of uncoated 316L, gold-coated 316L and graphite as a function of the temperature of cell, while holding a constant clamping pressure and a constant current density. All three materials show a significant decrease of the contact resistance with increasing temperature, showing that the contact resistance is in fact strongly temperature dependent. Furthermore, additional measurements carried out by cycling the temperature between 25 and 80 °C further revealed that the contact resistance is not completely reversible. The inset of Fig. 8 shows that the contact resistance of the uncoated 316L has a large degree of hysteresis as the temperature is once again lowered. This result may indicate that the temperature affects the effective contact area between GDL and BPP rather than the electronic properties of the materials, which should be a fully reversible phenomenon.

Humidified gases and the presence of liquid water are in most cases unavoidable conditions inside PEMFCs. Fig. 9a–c shows the ex-situ contact resistance of the three materials simulating flooding conditions. The experiment was carried by changing the oxygen

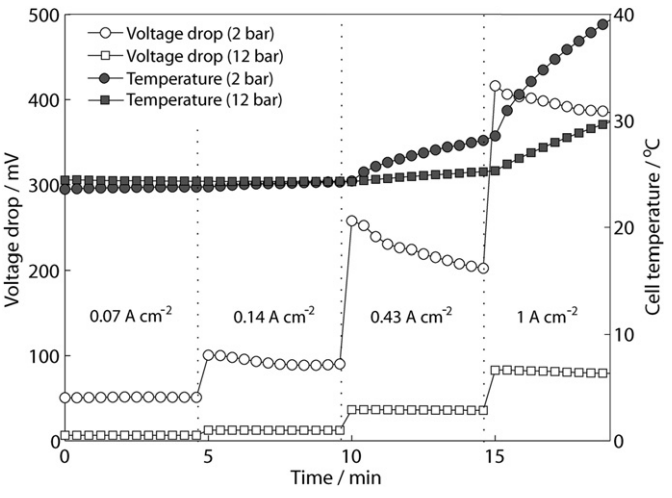

Fig. 7. Transient measurement of the voltage drop between uncoated 316L and GDL Sigracet 10 BC at 2 bar and 12 bar clamping pressure. The temperature is recorded with temperature probe C (see Fig. 1b).

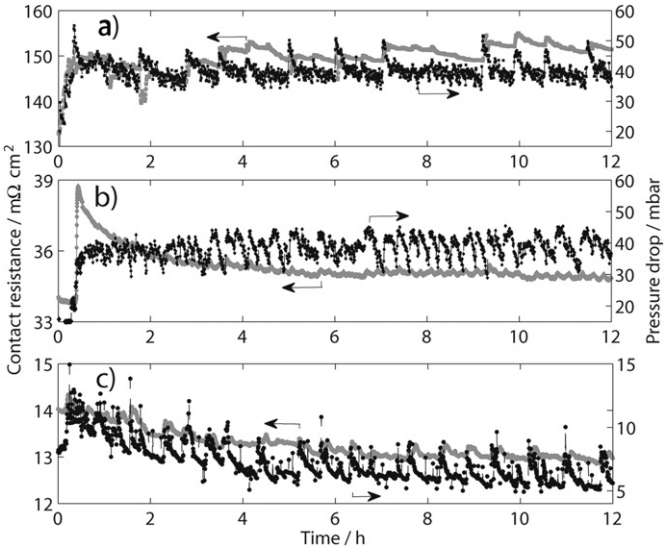

Fig. 9. Ex-situ contact resistance in the presences of oversaturated O_2. The measurement is carried out at clamping pressure 8 bar, cell temperature 80 °C, gas dew point 84 °C, O_2 flow rate 60 ml min^{-1}, current density 0.143 A cm^{-2} and using GDL Sigracet 10 BC. Contact resistance and pressure drop for: a) uncoated 316L, b) gold-coated 316L and c) graphite.

flow from completely dry to oversaturated by water within the first 30 min of the experiment and later maintained at constant high water content for the remaining time. The introduction of humidified oxygen not only increases the pressure drop over the flow field/GDL, but it also appears to affect the contact resistance, especially for uncoated 316L. Several hours into the measurement it is also possible to observe oscillatory changes in pressure drop. These changes are attributed to the condensation and removal of liquid water in the flow field/GDL. Interestingly, the contact resistance appears to change synchronously with all large changes in pressure drop, implying that the presence of liquid water may alter the effective contact area between GDL and BPP.

3.3. In-situ contact resistance

3.3.1. The effect of temperature

Fig. 10a shows the cell voltage, the HFR-corrected cell voltage and the pressure drop at the cathode as function of operating temperature at 0.143 A cm^{-2} using completely dry H_2 and O_2. There is a significant difference in cell voltage between uncoated 316L and graphite, a difference that increases with increasing operating temperature. The HFR-corrected cell voltage reveals that ohmic losses are indeed the largest contribution to this difference and where the HFR represents the total ohmic resistance of the cell, including the contribution of the contact resistance. Fig. 10b in turn shows that the HFR is about one order of magnitude larger than the contact resistances under these dry conditions and while the HFR increases exponentially with increasing temperature, the contact resistance, just as in the ex-situ measurements in simulated environment, has a clear tendency to decrease. Fig. 10b also highlights the degree of difficulty of evaluating BPP materials in-situ, without the direct measurement of the contact resistance. It is observed that the differences in contact resistance between uncoated 316L and graphite do not account for the large differences in HFR between the two cells. On the other hand, significant differences in water management between the cells are possible to observe from EIS.

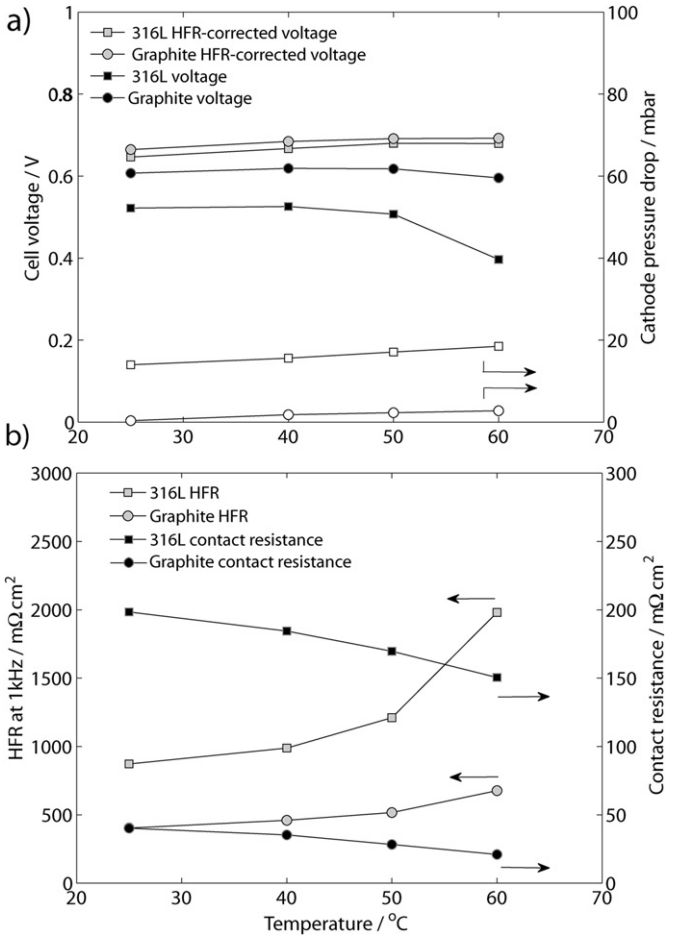

Fig. 10. In-situ measurements with dry O_2 and H_2, flow rate 60 ml min^{-1} for both O_2 and H_2, clamping pressure 8 bar, GDL Sigracet 10 BC at both anode and cathode and a constant current density of 0.143 A cm^2. Due to the extremely dry conditions, at least 1 h of steady state operation was needed for each particular measurement. a) Effect of temperature on cell voltage, HFR-corrected cell voltage and pressure drop at cathode and b) effect of temperature on the contact resistance and HFR.

Fig. 11 shows the EIS measurements at 27 and 60 °C. At the present operating conditions e.g. dry pure gases and high stoichiometry, the capacitive semi-circles at intermediate frequencies (10 kHz–1 Hz), are mainly coupled to different processes at the cathode catalyst layer. These semi-circles are similar in magnitude at the same temperature and correspond to similar Tafel slopes of the oxygen reduction reaction (ORR) [25]. The impedance spectra of uncoated 316L have on the other hand an extended 45 °C branch at high frequencies (10 kHz–1 kHz) which is mainly associated to a higher ionomer resistance [26,27]. An additional sign that the cell using uncoated 316L steel has deficiencies in water management is that the impedance spectrum at 60 °C shows an additional capacitive semi-circle at low frequencies (top frequency 1 Hz). This part of the impedance spectra is mainly coupled to dehydration of the anode due to limited back transport of water through the membrane [28,29]. Even though the surface hydrophobicity of the BPP has been reported to have effect on the water balances of the cell, it is worth recalling that the uncoated 316L steel sample used in this study also has shallower BPP channels than graphite. Shallower channels not only increases the pressure drop at the cathode (see Fig. 10a), but the higher gas velocity may also causes severe drying of the polymeric phase at low RH.

3.3.2. The effect of humidity

Fig. 12a shows the cell voltage, the HFR-corrected cell voltage and the pressure drop at the cathode as a function of the RH of the gases at 0.143 A cm^{-2}. Despite the previously measured differences in contact resistance, the difference in cell voltage between uncoated 316L steel and graphite is small, especially at low RH. This is

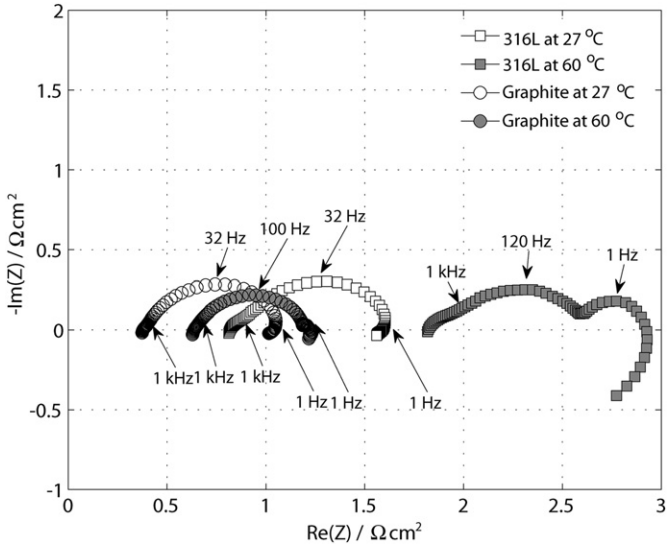

Fig. 11. Nyquist plot of EIS measurements using dry O_2 and H_2, current density 0.143 A cm^{-2}. Conditions as in Fig. 10.

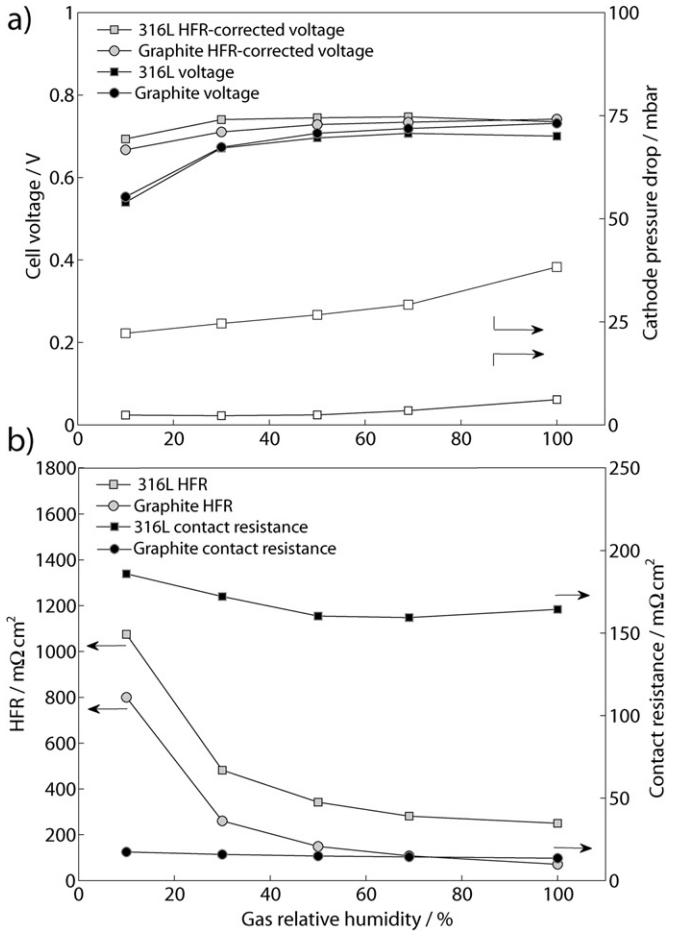

Fig. 12. In-situ measurements with humidified O_2 and H_2, cell temperature 80 °C, flow rate 60 ml min^{-1} for both O_2 and H_2, clamping pressure 8 bar, GDL Sigracet 10 BC at both anode and cathode and a constant current density of 0.143 A cm^2. At least 1 h of steady state operation was used for each particular measurement. a) Effect of RH on cell voltage, HFR-corrected cell voltage and pressure drop at cathode and b) effect of RH on the contact resistance and HFR.

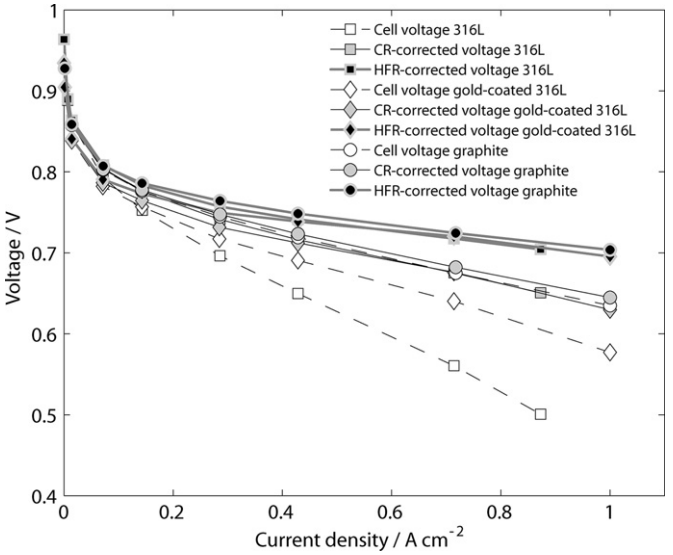

Fig. 13. Steady state polarization curves. Each plotted point is the last recorded value of a 15 min measurement. Conditions: 100% RH O_2 and H_2, cell temperature 80 °C, flow rate 60 ml min^{-1} for both O_2 and H_2, clamping pressure 8 bar, Sigracet 10 BC at both anode and cathode.

probably caused by small differences in electrode performance when restarting the fuel cell after an overnight recess and further highlights the degree of difficulty of evaluating BPP materials in-situ without the direct measurement of the contact resistance. The HFR-corrected cell voltages in Fig. 12a indeed confirms that the fuel cell using uncoated 316L has slightly better electrode performance up to 70% RH. At 100% RH on the other hand, the cells show instead the same electrode performance and the ohmic losses are here the main contributor to the observed differences in voltage.

Fig. 12b displays a nearly exponential decrease of the HFR as the ionic conductivity of the membrane and electrodes improves with increasing RH. Fig. 12b also reveals that a small part of the decrease in HFR is in fact due to a decrease in contact resistance. Increasing the RH of the gases not only changes the water content in the membrane, but it may also change its thickness, resulting in the compression of the GDL. However, the contact resistance of uncoated 316L stops decreasing at 50% RH and instead increases at high RH and high pressure drop at the cathode, similarly to what was observed during the ex-situ measurements in the presence of liquid water.

3.3.3. The effect of current density

Fig. 13 shows steady state polarization curves taken after approximately 40 h of constant current operation. At open circuit voltage (OCV) there are only small differences in cell voltage between the set-ups and since no current is drawn from the cell, there are obviously no losses due to contact resistance. At 0.143 A cm^{-2} the differences in performance are still small, the cell voltages are 0.75 V, 0.76 V and 0.78 V, for uncoated 316L, gold-coated 316L and graphite, respectively and do not exactly correspond to the differences in contact resistance. At higher current densities, e.g. 0.71 A cm^{-2}, the differences in performance become more significant, with cell voltages of 0.56 V, 0.64 V and 0.68 V for uncoated 316L, gold-coated 316L and graphite, respectively. Furthermore, at this current density, the contact resistance-corrected cell voltages are 0.675 V, 0.676 V and 0.682 V for uncoated 316L, gold-coated 316L steel and graphite, respectively, showing that under these particular operating conditions the dominant contribution to the difference in cell voltage is indeed the contact resistance.

Fig. 14 shows the transient of the cell voltage, voltage drop between BPP and GDL, cell temperature and pressure drop during the execution of the polarization curves shown in Fig. 13. It is not possible to observe any clear correlation between the temperature and voltage drop transients, probably because the changes in temperature are not significant enough. For uncoated 316L and gold-coated 316L it is however possible to observe a simultaneous increase in voltage drop and pressure drop during the 0.71 A cm^{-2} transient. The increased water production at the cathode, combined with the smaller channel dimensions of these samples, increases the pressure drop from 40 mbar to approximately 60 mbar. The changes in voltage drop during the 0.71 A cm^{-2} transient could be considered negligible in the case of graphite (0.29 mV or 0.41 mΩ cm^2). For gold-coated 316L, only a slightly larger increase is observed (1 mV or 1.4 mΩ cm^2). The uncoated 316L on the other hand, which is more sensitive to changes in the effective contact area, experience a considerably larger increase (8 mV or 11 mΩ cm^2).

3.3.4. Contact resistance during long-term operation

Fig. 15 shows the cell voltage and the contact resistance during a 100 h measurement that, with the exception of performed polarization curves, seen as discontinuities, was operated at

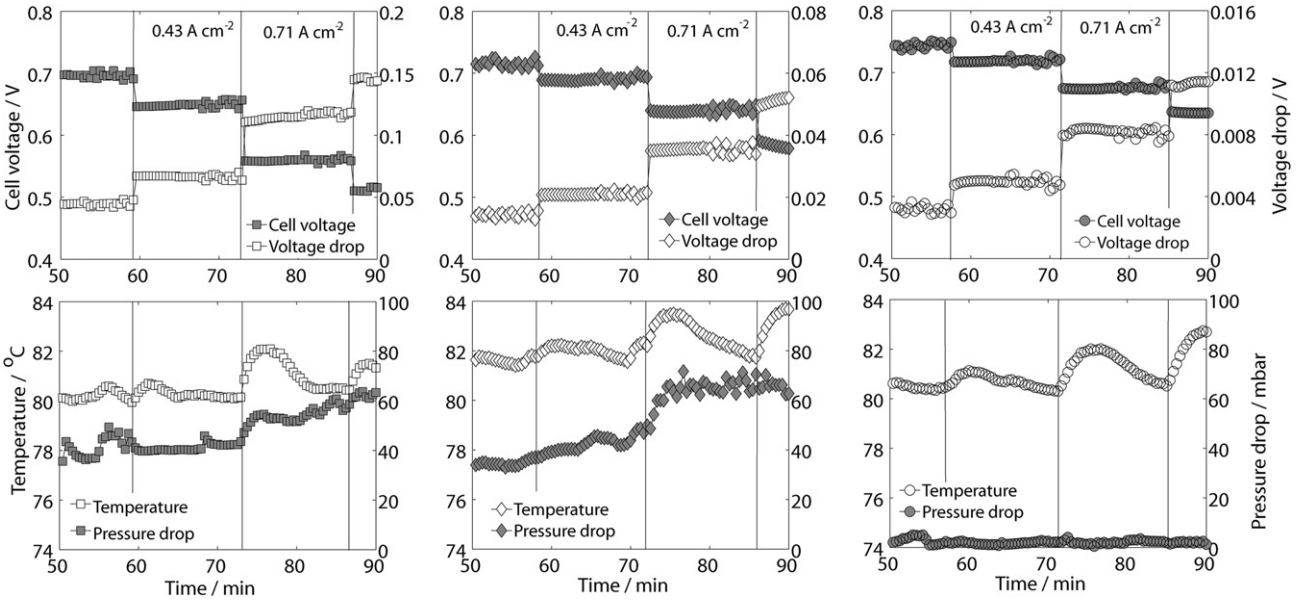

Fig. 14. Transients of cell voltage and voltage drop between BPP and GDL (*above*). Transients of cell temperature and pressure drop at the cathode (*below*). The transients are measured during the polarization curve seen in Fig. 13 for: a) uncoated 316L, b) gold-coated 316L and c) graphite.

a constant current density of 0.143 A cm^{-2}. After high current density operation the contact resistance changes to a new level, especially for uncoated 316L, but also for the gold-coated 316L. Changes in cell voltage due to changes in contact resistance are not only difficult to observe since the cells are operated at low current densities, but also because after each performed polarization curve the cell voltage experiences an improvement. This improvement is mainly attributed to improved ionic conductivity of membrane and electrodes, as well as improved electrode kinetics upon high current density operation. All three samples experience an overall increase in contact resistance. While the contact resistance of graphite increases from 10.4 to 11.1 mΩ cm^2, the contact resistances of gold-coated 316L and uncoated 316L steel increase from 45 to 64 mΩ cm^2 and from 141 to 170 mΩ cm^2, respectively. This result shows that significant irreversible changes to the contact resistance may occur during long-term operation.

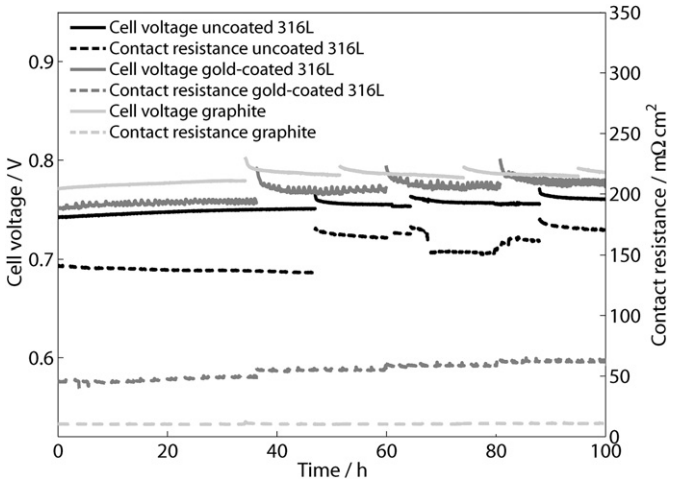

Fig. 15. In-situ measurements at a constant current density of 0.143 A cm^{-2}. Conditions as in Fig. 13.

4. Discussion

As it is seen in Figs. 8 and 10, there is a clear decrease of the contact resistance with increasing temperature for all three BPP materials. The dependence on temperature may in turn be a combined effect of several phenomena, including changes in electric conductivity of the passive film, gold-coating, bulk of the stainless steel, graphite current collectors and GDL graphitic fibers. However, the largest contribution is most certainly due to the thermal expansion of the components inside the cell, compressing the GDL and enlarging the effective contact area between BPP and GDL, agreeing with the simulated results of Y. Zhou et al. [30]. Furthermore, the inset of Fig. 8 shows that temperature cycling causes a large degree of hysteresis on the value of the contact resistance, an expected result considering the thermal expansion mechanism. Temperature cycling is in this context directly related to compression cycling of the GDL, which is known to undergo irreversible deformation upon compression [31].

The in-situ measurements show a small decrease in contact resistance with increasing RH of the gases for both graphite and uncoated 316L (see Fig. 12). This is attributed to the water uptake of the membrane and its ability to swell with increasing water content [32]. An increased membrane thickness results in the deformation of the GDL, increasing the effective contact area between BPP and GDL and decreasing the contact resistance, which is also in agreement with modeling results of Y. Zhou et al. [30].

It is not straightforward to predict the effect of current density on the in-situ contact resistance, because there is a simultaneous increase in heat and water production. From the ex-situ measurements in simulated environment, without the presence of an MEA (see Figs. 6 and 7), it is argued that the contact resistance is dependent on current density through its strong dependence on temperature. Thus, the contact resistance decreases due to thermal expansion of the materials. However, during in-situ operation at high cell temperature and high current density, e.g. 80 °C and 0.71 A cm^{-2}, the measured temperature rise due to ohmic resistances, entropic heat of reaction, irreversibilities of the electrochemical reactions and water condensation is only a few degrees and is not enough to have a significant effect on the contact resistance.

High water content in the cathode compartment, which in this study is measured as an increase in pressure drop, generally causes an increase of the contact resistance. This was shown during the ex-situ measurements in simulated environment using over-saturated oxygen (Fig. 9), at high RH during the humidity sweep in the in-situ measurements (Fig. 12) and at high current densities during the execution of the polarization curves (Fig. 14). Although it is very challenging to establish the exact cause behind the increase in contact resistance at high water content, three mechanisms may be considered as possible: *i*) liquid water directly involved in blocking the electronic path between GDL and BPP, *ii*) forces acting on the land of the BPP during the discharge of liquid water from the GDL and *iii*) forces acting on the GDL due to the buildup of gas pressure during the removal of water droplets from the channel of the BPP. To the authors' best knowledge, such mechanisms have not been presented in the literature and it is at this stage unclear if these mechanisms actually occur in a PEMFC. It is however believed that Milli-Q water, used to humidify the gas stream, might be resistive enough to alter the electronic path and to consider mechanism *i*) as possible. Studies of water transport in GDL and water discharge into the BPP using visualization techniques such synchrotron X-ray radiography also opens for the possibility to consider mechanism *ii*) as possible. It has been observed that one of the main mechanisms for water discharge is the significant accumulation of liquid water under the land and a subsequent ejection into the channel [33–35]. Furthermore, it is suggested that mechanism *iii*) might be in agreement with the observations made by Ihonen et al. [21], which measured an increase of the contact resistance of stainless steel 316L when raising the gas pressure, proposing that a high enough gas pressure could reduce the effective contact area between GDL and BPP and increase the contact resistance.

Considering the dynamic nature of the passive film on stainless steels, time may also plays an important role in the stability of the contact resistance. Fig. 9a reviled that when the changes in pressure drop are sufficiently fast, e.g. when the condensed water in the flow field or in the GDL is rapidly removed, the effective contact area is fully re-established before affecting the properties of the passive film of the steel. However, during long periods at high current densities, e.g. during the execution of polarization curves, the newly exposed contact spots may have sufficient time of exposure to the fuel cell environment to also increase the rate of oxide growth and permanently affected the contact resistance.

During long-term operation (see Fig. 15), it was also possible to observe an increase in contact resistance of the gold-coated 316L, as well as for graphite. Although post-mortem analysis of the fuel cell components was out of the scope of this study, coating degradation and GDL degradation cannot be discarded as possible causes. These results highlight the significance of the in-situ technique used in this study. The direct measurement of the contact resistance becomes essential to be able to identifying and separating this particular source of voltage loss from other possible ohmic losses such as membrane resistance or electrode ionomer resistances, especially when it has previously been reported that membrane resistance may significantly increase due to metal ion poisoning [5]. Furthermore, ongoing lifetime testing that will be included in a forthcoming publication have shown that the contact resistance between BPP and GDL may increase to unacceptable levels when cycling to high current densities for extended periods of time.

5. Conclusions

The effective contact area between GDL and BPP is crucial for the magnitude and stability of the contact resistance, especially for poorly conductive materials such as uncoated stainless steels. The contact resistance between BPP and GDL decreases with increasing temperatures, independently of the material and probably due to thermal expansion of the components inside the cell. The contact resistance is affected positively by an increased RH of the gases, probably due to increased membrane thickness. On the other hand, both the ex-situ measurements in simulated environment and the in-situ measurements show that liquid water, measured as an increase in pressure drop, affects the contact resistance negatively, especially for materials with high initial contact resistance and materials with dynamic surface properties, such as uncoated stainless steels. Finally, current density seems to have a dual effect on the contact resistance. While an increased current density may decrease the contact resistance due to an increase in temperature, especially at low clamping pressures, it may also increase the contact resistance due to water production. In the case of uncoated 316L and gold-coated 316L, high current density operation for extended periods of time also causes a progressive deterioration of the contact resistance. These changes could have been mistaken for other ohmic losses, such as metal ion poisoning of membrane and ionomer if the direct measurement of the contact resistance had not been carried out.

Acknowledgment

The financial support from the Swedish Foundation for Strategic Environmental Research (MISTRA), Program Council for Vehicle related research (PFF), and the Swedish Research Council (VR) are gratefully acknowledged.

References

[1] J.S. Cooper, J. Power Sources 129 (2004) 152–169.
[2] P.L. Hentall, J.B. Lakeman, G.O. Mepste, P.L. Adcock, J.M. Moore, J. Power Sources 80 (1999) 235–241.
[3] D.P. Davies, P.L. Adcock, M. Turpin, S.J. Rowen, J. Power Sources 86 (2000) 237–242.
[4] S.-H. Wang, J. Peng, W.-B. Lui, J.-S. Zhang, J. Power Sources 162 (2006) 486–491.
[5] A. Pozio, R.F. Silva, M. De Francesco, L. Giorgio, Electrochim. Acta 48 (2003) 1543–1549.
[6] J. Wind, R. Späh, W. Kaiser, G. Böhm, J. Power Sources 105 (2002) 256–260.
[7] H. Wang, M.A. Sweikart, J.A. Turner, J. Power Sources 115 (2003) 243–251.
[8] D.P. Davies, P.L. Adcock, M. Turpin, S.J. Rowen, J. Appl. Electrochem. 30 (2000) 101–105.
[9] N. Cunningham, D. Guay, J.P. Dodelet, Y. Meng, A.R. Hlil, A.S. Hayb, J. Electrochem. Soc. 149 (2002) A905–A911.
[10] S. Kitta, H. Uchida, M. Watanabe, Electrochim. Acta 53 (2007) 2025–2033.
[11] T.J. Toops, M.P. Brady, P.F. Tortorelli, J.A. Pihl, F. Estevez, D. Connors, F. Garzon, T. Rockward, D. Gervasio, W. Mylan, S.H. Kosaraju, J. Power Sources 195 (2010) 5619–5627.
[12] A. Kraytsberg, M. Auinat, Y. Elin-Eli, J. Power Sources 164 (2007) 697–703.
[13] J. André, L. Antoni, J.-P. Petit, E.D. Vito, A. Montani, Int. J. Hydrogen Energy 34 (2009) 3125–3133.
[14] R.F. Silva, D. Franchi, A. Leone, L. Pilloni, A. Masci, A. Pozio, Electrochim. Acta 51 (2006) 3592–3598.
[15] D.-G. Nam, H.-C. Lee, J. Power Sources 170 (2007) 268–274.
[16] K. Feng, T. Hu, X. Cai, Z. Li, P.K. Chu, J. Power Sources 199 (2012) 207–213.
[17] Y. Mori, M. Ueda, M. Hashimoto, Y. Aoi, S. Tanase, T. Sakai, Surf. Coat. Technol. 202 (2008) 4094–4101.
[18] P. Yi, L. Peng, L. Feng, P. Gan, X. Lai, J. Power Sources 195 (2010) 7061–7066.
[19] M. Kumagai, S.-T. Myung, T. Ichikawa, H. Yashiro, J. Power Sources 195 (2010) 5501–5507.
[20] R.C. Makkus, A.H.H. Janssen, F.A. De Bruijn, R.K.A.M. Mallant, J. Power Sources 86 (2000) 274–282.
[21] J. Ihonen, F. Jaouen, G. Lindbergh, G. Sundholm, Electrochim. Acta 46 (2001) 2899–2911.
[22] A. Oyarce, N. Holmström, A. Bodén, S. Randström, G. Lindbergh, ECS Trans. 25 (2009) 1791–1801.
[23] S. Randström, C. Lagergren, P. Capobianco, J. Power Sources 160 (2006) 782–788.
[24] N. Holmström, J. Ihonen, A. Lundblad, G. Lindbergh, Fuel Cells 4 (2007) 306–313.
[25] F. Jaouen, G. Lindbergh, J. Electrochem. Soc. 150 (12) (2003) A1699–A1710.
[26] R. Makharia, M.F. Mathias, D.R. Baker, J. Electrochem. Soc. 152 (2005) A970–A977.

[27] F. Jaouen, G. Lindbergh, K. Wiezell, J. Electrochem. Soc. 150 (12) (2003) A1711–A1717.
[28] N. Holmström, K. Wiezell, G. Lindbergh, J. Electrochem. Soc. 159 (8) (2012) F369–F378.
[29] I.A. Schneider, H. Kuhn, A. Wokaun, G.G. Scherer, J. Electrochem. Soc. 152 (12) (2005) A2383.
[30] Y. Zhou, G. Lin, A.J. Shih, S.J. Hu, J. Power Sources 192 (2009) 544–551.
[31] V. Radhakrishnan, P. Haridoss, Int. J. Hydrogen Energy 35 (2010) 11107–11118.
[32] Y. Tang, A.M. Karlsson, M.H. Santare, M. Gilbert, S. Cleghorn, W.B. Johnson, Mater. Sci. Eng. A 425 (2006) 297–304.
[33] P. Deevanhxay, T. Sasabe, S. Tsushima, S. Hirai, Int. J. Hydrogen Energy 36 (2011) 10901–10907.
[34] I. Manke, Ch. Hartnig, M. Grünerbel, W. Lehnert, N. Kardjilov, A. Haibel, A. Hilger, J. Banhart, H. Riesemeier, Appl. Phys. Lett. 90 (2007) 174105.
[35] T. Sasabe, P. Deevanhxay, S. Tsushima, S. Hirai, J. Power Sources 196 (2011) 8197–8206.